Attraction and repulsion between objects in a granular flow

G. A. Caballero-Robledo [1,*] M. F. Acevedo-Escalante [1] F. Mandujano [2] and C. Málaga [2,†]
[1]*CINVESTAV-Monterrey, PIIT, Nuevo León, 66600, México*
[2]*Departamento de Física, Facultad de Ciencias, Universidad Nacional Autónoma de México, Ciudad Universitaria, C.P. 04510, Cd. de México, México*

(Received 22 September 2020; accepted 19 July 2021; published 13 August 2021)

The objective of this work is the understanding of lift forces exerted on two side-by-side intruders within a granular flow that is uniform upstream. To this end, we have performed experiments that reveal long-range attraction and repulsion depending on flow velocity and the distance between intruders. We found an interesting correlation between the asymmetry of flow velocity around the obstacles and the lift force, although the understanding of this correlation rests as an open question for future work. Additionally, a hydrodynamic model based on kinetic theory for inelastic particles was solved numerically. The model reproduces remarkably well the general qualitative features of the experiments which shows that the system behaves similarly to a pair of hot intruders immersed in a liquid of temperature-dependent viscosity. However, quantitative discrepancies suggest that better constitutive relations are needed.

DOI: 10.1103/PhysRevFluids.6.084303

I. INTRODUCTION

This work was motivated by a setup well used to explore hydrodynamic interactions between particles, drops, and bubbles in a fluid flow. [1]. Typically, the intruders are placed side by side in a uniform flow [see Fig. 1(b) for a schematic representation of the setup]. However, to the best of our knowledge, it has not been used before in the case of the flow of granular material. Only recently, our group performed numerical simulations using such a configuration [2].

For a steady viscous flow, at moderate Reynolds numbers (Re), a repulsive interaction is observed between objects placed side-by-side if they are close enough to each other [3]. The interaction changes sign and becomes a weak attraction as objects move apart. As Re decreases, repulsion increases, and you need to move them farther apart to observe an attractive interaction. This attraction grows weaker as Re tends to zero, and the flow approaches the Stokes limit. This behavior indicates that the attractive interaction is originated from the inertia of the fluid (a Bernoulli effect), and therefore accentuated at larger Re, while viscosity governs repulsive forces [4].

In the case of intruders in a granular flow, drag has received more attention than lift. It appears that at slow flows, drag is independent of the granular media velocity, while it is proportional to the square of this speed if the granular media is moving fast [5–8]. Nonetheless, intruders in a granular flow do experience long range interactions, for example, in segregation processes [9–16]. Attraction and repulsion has been observed between objects placed side-by-side within granular flows, and in some cases it has been suggested that some of these forces follow Bernoulli equation for irrotational fluids [14,16,17].

*g.a.caballero.robledo@gmail.com
†cmi.ciencias@ciencias.unam.mx

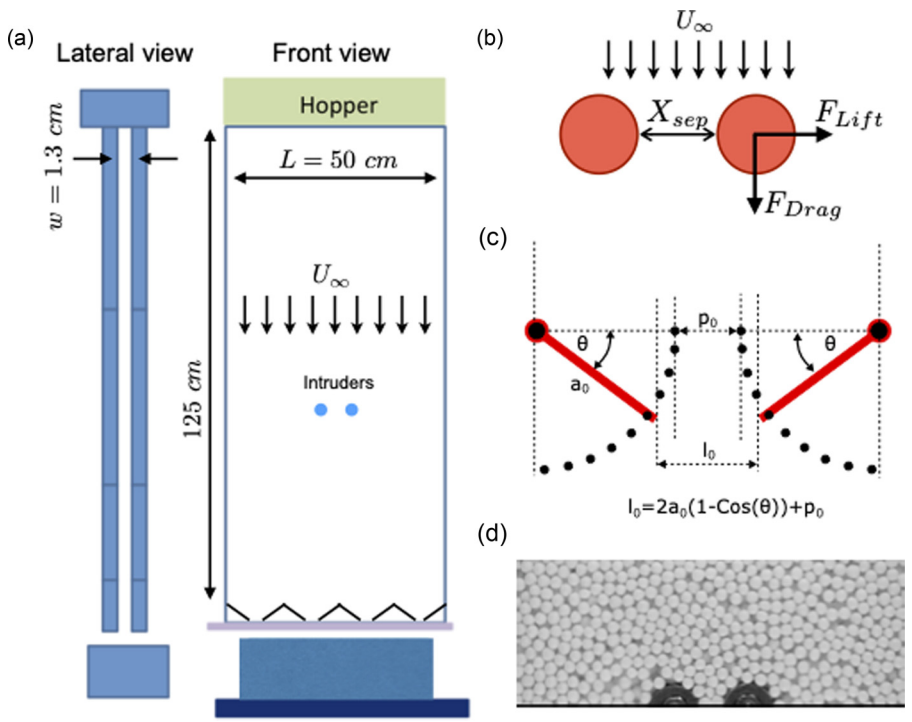

FIG. 1. (a) Schematic representation of the experimental setup. Big, thick polycarbonate sheets placed face-to-face, 1.3 cm apart from each other form a quasi-two-dimensional container. The container is filled with tapioca seeds of diameter $d = 0.33 \pm 0.02$ cm and density $\rho_t \approx 2.7$ g/cm^3. (b) Two cylindrical obstacles of diameter $D = 1.5$ cm are placed side-by-side between the walls of the container without touching them, 55 cm above the bottom. The gap between the cylinders X_{sep} can be varied, and the cylinders are attached to force gauges that allow measuring the vertical, F_{Drag}, and horizontal, F_{Lift}, forces on them. (c) The angle of tilted sticks placed at the bottom of the container controls mass flow out of the system. (d) Front view of the intruders immersed in the granular medium before the flow begins. See Supplemental Material [24] for more details.

Inspired by experiments of Pacheco-Vázquez and Ruiz-Suárez [16], Solano-Altamirano *et al.* [18] performed granular experiments and 2D simulations where a group of massive intruders fall and penetrate an extremely lightweight granular media in the presence of gravity. It was found that repulsion depended on jamming, and attraction seemed to be a Bernoulli-like effect. Unfortunately, intruders' relative speed and the dependence of the dynamics on depth and time made the interactions too complicated and difficult to understand.

To overcome these complications, López de la Cruz and Caballero-Robledo [2] decided to work numerically with a pair of fixed circular intruders immersed on a 2D granular flow driven by gravity, the setup of the present work. Their findings revealed remarkable features about the intruders' interactions. In the search for a Bernoulli-like effect, they tried to correlate the lift force and the difference in grains' average speed on both sides of the intruder. Surprisingly, the best correlation resulted when averages where taken, not at both sides of the intruders' equator (considering the equator on the line between the intruders' centers), but at 45 degrees above the equator in the upstream direction (see Fig. 3). Additionally, the lift seemed to depend on the speed square difference divided by the upstream granular speed to the power of $3/2$, an unexpected feature. The authors concluded that the origin of the attractive lift did not seem to be a Bernoulli-like effect and suggested using Coulomb's theory for passive failure [19] to describe the system. Alternatively, an extension of kinetic theory

to dense granular flows [20], or local rheology based on the nondimensional shear rate I [21] could also be apt.

More recently, Dhiman *et al.* [17] performed numerical simulations of two spheres moving horizontally side-by-side in a box with periodic boundary conditions in the direction of the displacement. The lift force measured as a function of the separation between intruders and as a function of displacement velocity behaved similarly to the lift force reported in by López de la Cruz and Caballero-Robledo [2]. Moreover, the authors managed to qualitatively reproduce the lift force as a function of the intruders' separation. They do this by modeling a pressure on the intruders proportional to the difference of the local squared velocity at a contact point and the squared bulk flow velocity, but only if the contact point was part of a force chain. The authors rationalize such a model as Bernoulli's principle integrated with force chains. Unfortunately, they only test the model at a single value of the velocity, so it is not possible to know how it behaves at larger or lower velocities, which makes it challenging to evaluate the pertinence of interpreting the model as a Bernoulli effect.

Asking if a Bernoulli-like effect governs the interaction between intruders in a granular flow is equivalent to asking how much does the granular flow behaves like a fluid. We have seen that the behavior is not the same as in a viscous fluid, but it has been proposed by Seguin *et al.* [20] that it could be equivalent to hot intruders immersed in a model viscous fluid whose viscosity is sensitive to temperature variations [22,23]. The authors support this idea with experiments of a cylinder penetrating vertically in a static granular bed.

In this work, we present for the first time experimental results of long-range interactions between two objects placed side-by-side and immersed in a gravity-driven granular flow. We found the same attractive and repulsive regimes previously reported using numerical simulations. Specifically, attractive interaction increases as the upstream flow velocity decreases, contrary to what is observed in Newtonian fluid; and the intruders separation where the transition from repulsion to attraction is observed in a granular flow decreases (and seems to converge) as the upstream velocity decreases, as opposed to what is observed in a Newtonian fluid. Additionally, we found numerically that the forces computed with the model proposed by Seguin *et al.* [20] follow the trends observed in the granular experiment. It is remarkable that the continuum model, although only qualitatively, can reproduce features of the interaction that are completely different to those observed in a Newtonian fluid.

II. EXPERIMENTAL SETUP

The experimental setup (see Fig. 1) consists of a $125 \times 50 \times 1.3\ \mathrm{cm}^3$ container made of 2.54 cm thick polycarbonate sheets. The container is placed vertically and filled with dry tapioca seeds (diameter $d = 0.33 \pm 0.02$ cm and density $\rho_t \approx 2.7\ \mathrm{g/cm}^3$). Inclined plastic sticks placed at the bottom impede the free flow of the grains out of the container, imposing a constant discharge mass flow rate and, consequently, a constant flow velocity of grains inside the container. By varying the angle of the sticks, the flow velocity can be controlled (see Fig. S1 of the Supplemental Material [24] and Ref. [25]).

The tapioca seeds are poured into the container using a hopper placed at the top while a polycarbonate bar blocks the exit at the bottom. Six kilograms of seeds is enough to fill the box and part of the hopper. At the time $t = 0$, the bar at the bottom is removed, and the discharge of the tapioca begins. The tapioca falls into a second container placed on a weight scale, which allows monitoring the amount of discharged mass as a function of time [25].

Two cylindrical plastic obstacles of diameter $D = 1.5$ cm and 1.1 cm in length are placed side-by-side between the walls of the container without touching them at the height of 55 cm from the bottom. Thin ($\sim$3 mm), long screws which pass through small ($\sim$5 mm) holes in the polycarbonate sheets without touching them (see Fig. S2 of the Supplemental Material [24]) put the obstacles in place. The size of the gap between the cylinders, X_{sep}, can be varied thanks to a set of small holes placed all along the width of the polycarbonate sheet. We put thin adhesive tape on the inner part

of the container to close unused holes in a given experiment such that the flow of the grains is not affected by the holes.

Each cylindrical intruder is attached to a pair of force gauges (microload cell, 0–780 g, CZL616C, Phidgets Inc.) connected in series. The cylinder is connected to the gauge, which measures the horizontal (lift) force. The cylinder and the lift force gauge are attached to the vertical (drag) force gauge. All the system is fixed to an external aluminum support (see Fig. S2 of the Supplemental Material [24]). The cylindrical intruders and adapters for attaching the force gauges were designed and printed in a 3D printer (Replicator 2, MakerBot). 9V alkaline batteries power the force gauges, and the output voltage signal is read by an analog input card (9205 on cDAQ-9184, National Instruments) connected to the force gauges through a four-input PhidgetBridge circuit. All the system is connected to a physical ground to minimize the noise. Data acquisition is controlled through LabView (National Instruments) programs written by us. We calibrated the force gauges by attaching masses of known weight to them with the setup empty of grains.

Strong electrostatic forces are generated on the system due to the friction between grains and the polycarbonate walls during flow. These forces are eliminated by spraying an off-the-shelf antielectrostatic substance (antistatic screen cleaner, OfficeMax) on the polycarbonate sheets before assembling the container. During the experiments, the spray is distributed among all surfaces (tapioca seeds and walls) without affecting the flow of grains or the measured forces. After ten experiments, the antielectrostatic effect vanishes, and the system must be disassembled to respray the substance.

The flow of grains around the obstacles is filmed with a high-speed camera (Lightning RDT Plus) placed 30 cm away from the setup acquiring 512×512 pixels images at a rate of 250 frames per second. The movies are then analyzed using the particle image velocimetry (PIV)-ImageJ plugin, which measures the displacement of objects within a pair of images from the cross-correlation of subregions of the pictures. We work with subregions of 8×8 pixels, which have approximately the size of a single tapioca bead. From each consecutive pair of images, a velocity vector is obtained for each subregion. By averaging in time the velocity vectors on each region, the averaged velocity field of the flow of beads that are next to the front wall is obtained (see Fig. S4 of the Supplemental Material [24]). A granular temperature field is defined as the variance of the velocity on each subregion.

III. RESULTS AND DISCUSSION

Figure 2 shows the experimental results of the average lift force measured for different flow velocities, U_∞, and obstacles separations, X_{sep}. In the inset of Fig. 2(a), it is shown the raw data of the lift force as a function of time for a case of attractive lift. The signal is extremely noisy, and the force can have both positive (repulsion) and negative (attraction) values, but the smoothed signal shows that, on average, the net lift force is attractive [in previous simulations [18] we showed that the trajectory of a particle free to move through a granular medium is determined by the average of extremely fluctuating signals like the one shown in the inset of Fig. 2(a)]. The initial time $t = 0$ s corresponds to the moment when the bottom of the container opens, and the grains begin to flow. In this particular case, the force is constant and negative (attractive) for $t < 0$ s. This corresponds to the jammed state of the system that results from pouring the grains into the container. But in each experiment, the value of this initial force is different, and it can be repulsive, attractive or zero. It would be interesting to study this force in more detail. For $t > 0$ s, after a small transient, the force enters into a stationary state. It is in this state that we compute the average forces of the main plots in Fig. 2. The error bars of these data are obtained from the error of the mean of the force signals of both intruders and three repetitions of each experiment. At the end of the experiment, the force gradually diminishes, signaling the emptying of the container. When the container is empty, the measured force is zero. An interesting feature that our setup allows to study, but we have not done yet, is the possible correlations between the lift force experienced by both intruders simultaneously.

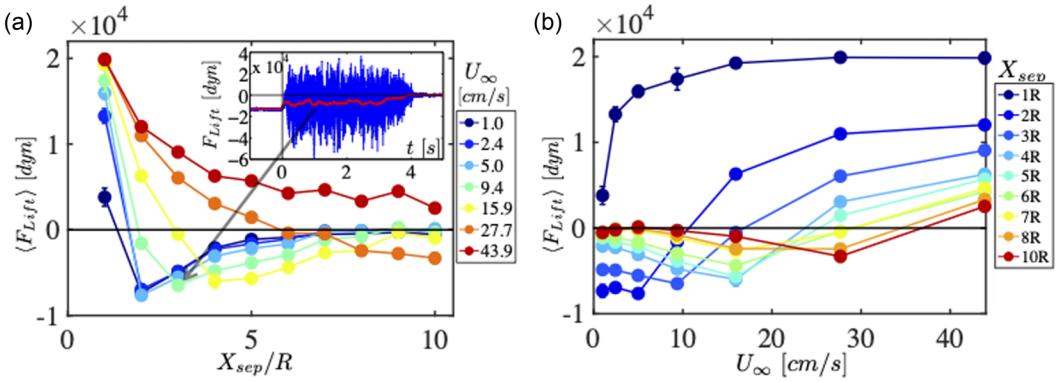

FIG. 2. (a) Mean value of the lift force as a function of the size of the gap between the intruders X_{sep}. $F_{\text{lift}} > 0$ means repulsion and $F_{\text{lift}} < 0$ attraction. Inset (a): Raw and smoothed data of the lift force as a function of time are plotted together for the left intruder for $U_\infty = 9.37$ cm/s and $X_{\text{sep}} = 3R$. The stationary state from which the mean force is calculated is clearly identified. (b) The same data as in panel (a) but presented as a function of the upstream flow velocity U_∞. The main plots include error bars, but for most of the points they are of the order of the size of the markers.

For the moment, we present in Fig. S4 of the Supplemental Material [24], the lift force as a function of time for both intruders.

The behavior of the lift force as a function of U_∞ and X_{sep} confirms what has been reported previously from numerical simulations [2,17], namely, that at a given separation of the obstacles, there can be attraction or repulsion between them depending on the flow velocity. If the obstacles are close, or the flow velocity is large, then repulsion is favored. In contrast, low flow velocities and moderate obstacles' separations enhance the attraction. The maximum attraction measured corresponds to a separation between obstacles equal to the diameter of an obstacle, i.e., $X_{\text{sep}} = 2R$. Interestingly, the attractive regime does not depend on flow velocity for $U_\infty < 5$ cm/s, which seems to be an indication that the system is in a quasistatic regime. However, one would then expect that repulsion would not depend on velocity either, which is not the case. Therefore, the nature of the mechanisms responsible for attraction and repulsion seem to be different.

Dense granular flows present different regimes which can be characterized by the Froude number Fr [8] or by the Inertia number I [21] (see the Supplemental Material [24] for the definition and estimation of the values of these two parameters in our experiments). When flow velocity is much smaller than rearrangements at the level of particles, the system is in a quasistatic regime, where forces do not depend on flow velocity (Fr < 0.1 or $I \to 0$ [26]). At large flow velocities (Fr > 10 or $I \gtrsim 1$), the system is in a rapid, dilute regime where forces change as the square of the velocity. In between, the system is in an intermediate regime where both gravity and inertia effects have comparable contributions [8,21]. Depending on the value of U_∞, in our experiments $0.03 <$ Fr < 1.2 and $0.01 < I < 0.4$. Interestingly, the transition form quasistatic to intermediate regime at Fr $= 0.1$ in our system corresponds to $U_\infty \approx 4$ cm/s. This transition can be clearly observed in Fig. 2(b), confirming that our system is in quasistatic regime for the lowest flow velocities.

An interesting question is the extent of the long-range interaction between the obstacles. In other words, at what separation do the obstacles do not see each other anymore. Figure 2 shows that this also depends both on the separation of obstacles and flow velocity. For small separations, the interaction between obstacles is strong, even at slow flow. In the quasistatic regime ($U_\infty < 5$ cm/s), Fig. 2(a) shows that the range of interaction goes from zero up to somewhere between $X_{\text{sep}} = 7R$ and $8R$. At larger velocities, the range of interaction depends on the flow velocity. For the largest separations that we tested, the obstacles do not see each other at small flow velocities. Then, at larger velocities, there is attraction and, finally, repulsion at the most substantial flow velocities.

The maximum flow velocity curve in Fig. 2(a) suggests that at larger separations, the lift force would probably decay to zero at around $X_{\text{sep}} \approx 15R$ without presenting an attractive regime, but this rests as speculation that we need to corroborate.

The drag force was measured using force gauges connected in series with the gauges for the lift force and the obstacles. Figure S3 of the Supplemental Material [24] shows the results. We did not find any apparent systematic behavior of the drag force as a function of obstacle separation or flow velocity. This result is at odds with the simulations previously reported [2,17], where the drag on a single obstacle is more extensive than when another obstacle is in proximity. This discrepancy between simulations and experiments should be further investigated. However, we suspect that connecting the force gauges in series in our experiments was not the right choice because the point of application of the force was too far from the measurement point, adding a nonnegligible torque and probably producing elastic deformations of the setup that interfere with the force measurement. For this reason, we think that our drag measurements are probably not precise enough and must be verified. This problem does not seem to have affected measurements of the lift, probably because the magnitude of the force in this direction is smaller. We noticed this unexpected behavior of the drag force only once the whole series of experiments were finished. In a future work we will study the drag force using a single gauge.

In a previous work by our group [2] we performed Discrete Soft Element simulations in a system similar to the one studied here and we found a strong correlation between the lift force and the quantity

$$\Delta\langle v\rangle^2 = \langle v(\text{out})\rangle^2 - \langle v(\text{in})\rangle^2, \tag{1}$$

where $\langle v(\text{in})\rangle$ and $\langle v(\text{out})\rangle$ are the average velocities of grains in the regions "in" and "out" of the gap between intruders and above them [see Fig. 3(c) for the definition of these regions]. We perform the same analysis here to verify that such correlation is also observed in the experiments. Figures 3(a) and 3(b) show examples of the average velocity field obtained from particle image velocimetry applied to the movies of the experiments. From these kind of velocity fields, we computed the quantity $\Delta\langle v\rangle^2$ defined in Eq. (1) using the regions "in" and "out" defined in Fig. 3(c). Similarly to what we found in our previous simulations, the best correlation with the lift force is obtained when $\Delta\langle v\rangle^2$ is divided by $U_\infty^{3/2}$, which can be verified by comparing Figs. 3(d) and 2(b) or, equivalently, from the excellent linear relationship observed between these quantities [see Fig. 3(e)]. The value of the exponent of U_∞ was found empirically (see Fig. S6 of the Supplemental Material [24] to see the comparison with other exponents) and, since we do not have any model to explain this scaling, we report this value as approximate, pending its exact determination for future works.

In the numerical simulations that we reported previously [2], we found a linear relation between the lift force and the "in" and "out" velocity difference divided by $U_\infty^{3/2}$, from which the following equation was proposed (Eq. (6.1) in Ref. [2]):

$$\langle F_{\text{lift}}\rangle = f_{\text{sim}}(\mu_{\text{eff}})\frac{\xi_{\text{sim}} S \rho_{\text{sim}} \phi \Delta\langle v\rangle^2}{\text{Fr}^{3/2}} + F_{(0,\text{sim})}, \tag{2}$$

where S is the projected area of the intruder, ρ_{sim} is the density of the granular material of the simulations, ϕ is the packing fraction and Fr is the Froude number (expressing flow velocity U_∞ as the Froude number has been shown to be pertinent for objects immersed in granular flows where gravity plays an important role [8]). $f_{\text{sim}}(\mu_{\text{eff}})$ and $F_{(0,\text{sim})}$ are the slope and the intercept that result from a linear regression to the data. $f_{\text{sim}}(\mu_{\text{eff}})$ is an unknown function of the friction coefficient μ_{eff}, and $F_{(0,\text{sim})}$ is an attractive force observed when $\Delta\langle v\rangle^2 = 0$. ξ_{sim} in Eq. (2) is a geometric factor which we could determine in the simulations by systematic variations of the width L of the system, the height h of the column above the obstacles, the diameter d of the particles, and the diameter D of the obstacles. For the two-dimensional simulations, ξ_{sim} is given by

$$\xi_{\text{sim}} = \left(\frac{h}{D}\right)\left(\frac{L}{D}\right)\left(\frac{D}{d}\right)^{1/2}. \tag{3}$$

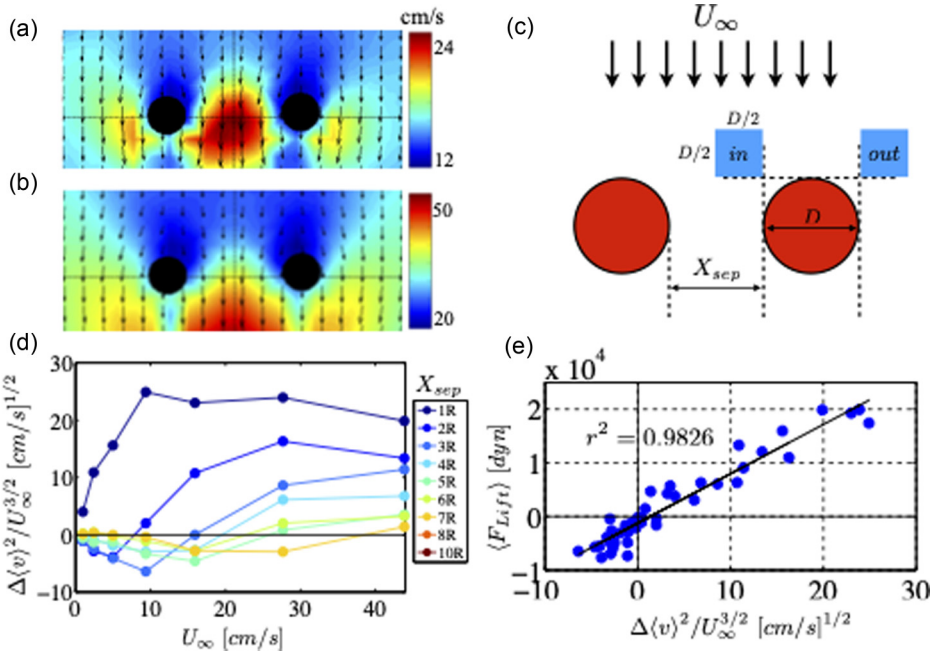

FIG. 3. (a) Attractive ($U_\infty = 15.9$ cm/s and $X_{\rm sep} = 5R$) and (b) repulsive ($U_\infty = 27.7$ cm/s and $X_{\rm sep} = 5R$) typical velocity fields obtained by applying particle image velocimetry (PIV) to the movies of the experiments (see Fig. S5 of the Supplemental Material [24] for an explanation of the procedure). (c) Schematic representations of the regions where the grains velocities were measured to compute the quantity $\Delta\langle v\rangle^2$ defined in Eq. (1). (d) $\Delta\langle v\rangle^2$ was computed from the velocity fields of the experiments and it was found that, when divided by $U_\infty^{3/2}$, its behavior was very similar to the behavior of the lift force shown in Fig. 2(b). (e) A good linear relation with a correlation coefficient of $r^2 = 0.9826$ is obtained when $\langle F_{\rm lift}\rangle$ is plotted as a function of $\Delta\langle v\rangle^2/U_\infty^{3/2}$.

In our experiments, we cannot determine the form of this geometrical factor because we have not yet varied these quantities Nevertheless, we can attempt to adapt Eq. (3) to our experimental system. The equation needs to be recast because there is a crucial difference between the simulations, that were two-dimensional, and the three-dimensional experiments. This difference makes the pressure around the obstacles to behave differently in the two systems. In the simulations, the pressure is a linear function of the height of the granular column above the obstacles, i.e., it behaves hydrostatically. In contrast, in the experiments, we expect the pressure at the level of the obstacles to be insensitive to the height of the granular column above them because the front and back walls would carry the weight of the column. This phenomenon is known as the Janssen effect. In essence, the pressure at the bottom as a function of the height of a granular column behaves hydrostatically for small heights, but it eventually saturates to a constant value. The height at which the pressure saturates is comparable to the horizontal size of the column. Therefore, in our experiments we expect that the pressure saturates at a height similar to w, the gap between the front and back walls, which is much smaller than the lateral size L of the container. Then, the geometrical factor $\xi_{\rm sim}$ that was determined in the simulations from dimensional analysis should be adapted to the experimental system as

$$\xi = \left(\frac{w}{D}\right)\left(\frac{L}{D}\right)\left(\frac{D}{d}\right)^{1/2}. \tag{4}$$

Noteworthy, the lateral walls in the experiments are much farther away from the intruders than in the simulations, therefore, it would not be surprising that the linear dependence on L would not be valid in our experimental setup.

Based on the linear growth observed in Fig. 3(e), we expect Eq. (2) to have the same form in our experiments as in the simulations, namely,

$$\langle F_{\text{lift}} \rangle = f(\mu_{\text{eff}}) \frac{\xi S \rho_t \phi \Delta \langle v \rangle^2}{\text{Fr}^{3/2}} + F_0, \tag{5}$$

where $\text{Fr} = U_\infty / \sqrt{gw}$ is the Froude number, $\rho_t \approx 2.7$ g/cm^3 is the density of tapioca, and $S = D \times w$ is the effective surface of the obstacles. Here we consider the packing density to be constant, $\phi = 0.6$. Although we do not have experimental measurements of ϕ, simulations suggested that its precise value did not play an important role in determining the value of the force. The nondimensional parameter $f(\mu_{\text{eff}})$ is expected to be a function of the effective friction of the granular material, defined as $\mu_{\text{eff}} = \tan(\theta)$, where $\theta = 35^\circ \pm 5^\circ$ is the angle of repose of tapioca. Data in Fig. 3(e) can be plotted in the form of Eq. (5) and the values of $f(\mu_{\text{eff}}) \approx 0.02$ and $F_0 \approx -1200$ dyn are obtained from linear regression. F_0 in Eq. (5) is the value of the lift force when $\Delta \langle v \rangle^2 = 0$ and, similarly to what we found in the simulations, it is attractive. The origin of this attractive force could be related to differences of velocity fluctuations at both sides of the intruders as suggested in other works [10,12,14]. It could also be an indication that the regions "in" and "out" where we are measuring the velocity are not the most pertinent. This force is something that we plan to study in the future. The magnitude of F_0 in our experiments is 13 times the weight of a grain $\rho_t g d^3$. Interestingly, in the simulations this ratio was of the same order of magnitude, $F_{(0,\text{sim})}$ was comparable to the weight of 20 grains, even though in the simulations we worked with a superlight granular material [16,18] with a density 200 times smaller than the density of tapioca. In our experiments, the ratio $\mu_{\text{eff}}/f(\mu_{\text{eff}})$ has a value between 30 and 40, while in the simulations it is approximately 10. This difference could be related to the need of a different function of L in Eq. (4). These results suggest that Eq. (5) is a good departure point to gain further insight into the mechanisms governing lift forces between two objects immersed in a granular flow. Concerning the flow regime, the experiments allowed us to explore a more extensive range of flow compared to the simulations. In terms of the Froude number, the range of the simulations was $0.1 < \text{Fr} < 0.5$, while the Inertia number had values in the interval $0.04 < I < 0.14$. Both ranges fall within the ranges of the experiments and suggest that the simulations are mostly inside the intermediate regime.

Another interesting quantity to analyze in our system is v_{mp}, the flow velocity at the middle point between intruders. Figure 4 shows v_{mp} as a function of the bulk velocity. There is an interesting relationship between this graph and the attractive and repulsive regimes observed in Fig. 2(b): when v_{mp} increases together with U_∞, there is attraction; in contrast, when U_∞ increases but v_{mp} remains constant, there is repulsion. We also found this behavior in our previous simulations [2], where we claim that the saturation of flow capacity in the gap between intruders is related to the jamming of an excess of grains trying to flow through the gap, pushing the obstacles away from each other and causing repulsion. Interestingly, whenever there is an attraction between the obstacles, v_{mp} is larger than the bulk velocity. However, there are cases of repulsion where this is also the case. See, for example, the case of 15.9 cm/s and $X_{\text{sep}} = 3R$ in Fig. 4. This feature is another indication that the attractive force is not a Bernoulli-like effect.

Granular temperature

The granular temperature is defined as [23]

$$T(x, z) = m \delta v^2, \tag{6}$$

where $\delta v^2(x, z) = \langle (v(x, z, t) - \langle v(x, z, t) \rangle)^2 \rangle$ is the variance of the velocity of particles and m is the mass of a single particle.

From particle image velocimetry, we can measure in our experiments the field map of the velocity variance. Figure 5(a) shows an example of the fields from which we computed the velocity variance, shown in Fig. 5(b). Figure 5(c) shows the velocity variance for different flow velocities along the line that passes through the equator of the obstacles. Therefore, it is possible to measure the velocity

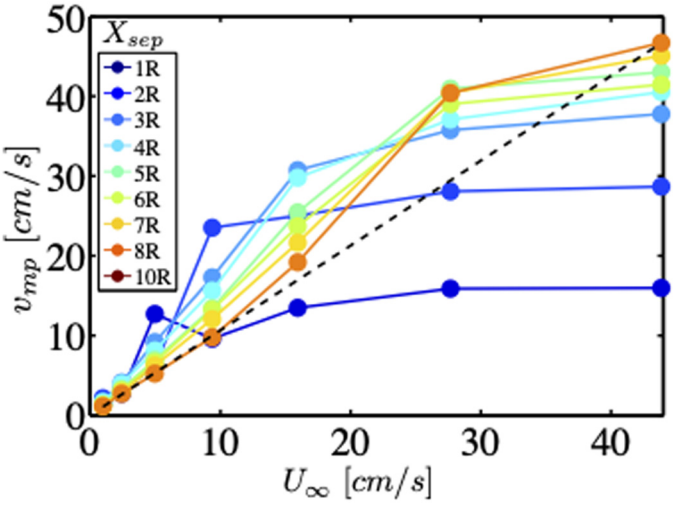

FIG. 4. Flow velocity in the middle point between obstacles, v_{mp}, plotted as a function of U_∞. The dashed line is the bulk flow velocity at the level of the equator of intruders.

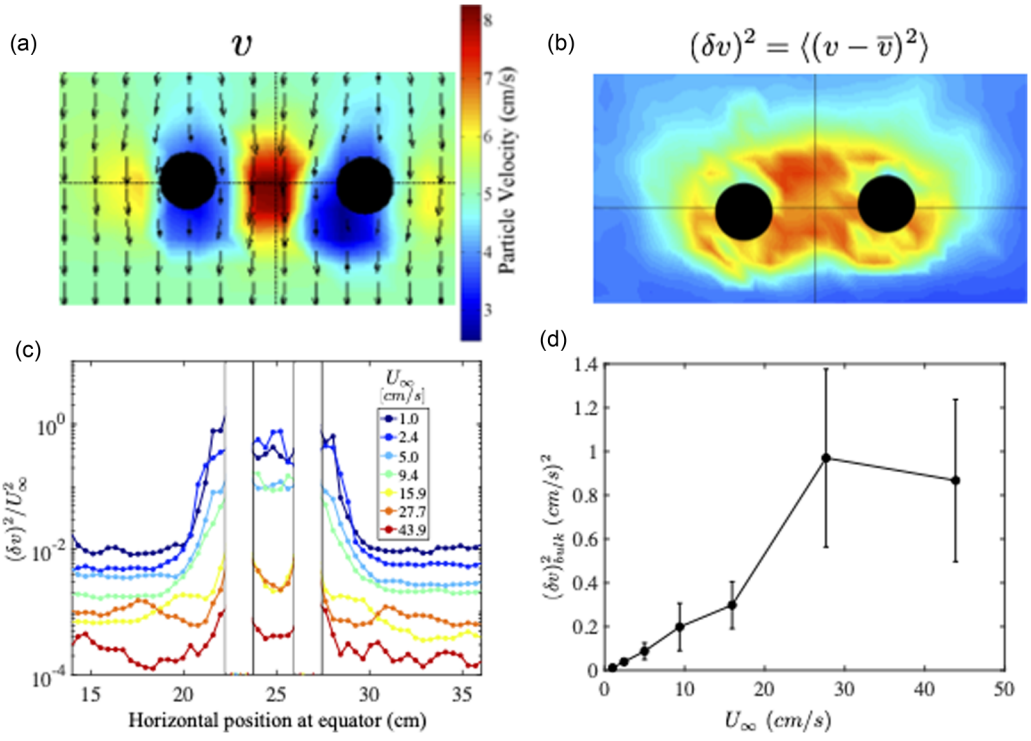

FIG. 5. (a) Velocity field and (b) Velocity variance (granular temperature) of the experiment for a case of attractive lift. (c) Velocity variance along the horizontal axis, which passes through the equator of intruders for different flow velocities. Vertical lines signal the position of the intruders, which, in this case, are separated by a distance of $X_{\mathrm{sep}} = 1.5D$. We obtained these data from images of the experiments like that shown in panel (b). Note that the region of analysis does not correspond to the limits of the experiment: the total width of the container is 50 cm. (d) Mean bulk velocity variance as a function of U_∞. The data was obtained from data like the one presented in panel (c) and averaged over all the experiments.

variance of the bulk as a function of U_∞. Figure 5(d) shows such a relation, which, apart from one data point, it seems to be linear. From a linear regression, we obtain

$$\delta v^2 \sim (2 \times 10^{-2} cm/s) U_\infty = U_0 U_\infty, \tag{7}$$

where we have defined a characteristic velocity $U_0 = 2 \times 10^{-2}$ cm/s whose meaning rests to be understood. If it is related to free fall under gravity, $U_0 = \sqrt{2gl}$, then it would define a characteristic distance $l \sim 2$ mm which is close to the size of the radius of the particles $d/2 = 1.65$ mm.

The experimental relation between velocity variance and U_∞, Eq. (7), allows to estimate the viscosity of the material and, therefore, the granular Reynolds number [23] (see the Supplemental Material [24] for the details of the granular Reynolds number estimation). We found that in our granular system the Reynolds number can be anywhere in the range $10^{-2} < \mathrm{Re} < 100$, although we guess that the most probable value is close to $\mathrm{Re} \sim 10$ (see the Supplemental Material [24]). This huge range reflects the fact that our estimation is based on imprecise assumptions and unknowns, especially the value of the packing fraction. Therefore, for the moment this estimation is useful only to compare the experimental results with the hydrodynamic model (see next section), and it should not be considered to determine the flow regime of the granular system. The inertia and Froude numbers are much better for that purpose.

IV. THE HYDRODYNAMIC MODEL

The hydrodynamic model used in the present work was proposed by Bocquet *et al.* [23] based on the kinetic theory for inelastic particles developed by Jenkins and Savage [22]. The flow of granular material is modeled by a fluid flow of variable viscosity as a function of temperature. Let $\boldsymbol{v}$ be the fluid velocity field, identified with the average granular velocity, and T the so called granular temperature, defined as the variance of the granular velocity. In the limit of incompressible flow, the model equations are

$$\rho \frac{D\boldsymbol{v}}{Dt} = \boldsymbol{\nabla} \cdot \boldsymbol{\sigma}, \tag{8}$$

$$\rho \frac{DT}{Dt} = \boldsymbol{\sigma} : \boldsymbol{e} + \boldsymbol{\nabla} \cdot (\lambda \boldsymbol{\nabla} T) - \epsilon T. \tag{9}$$

The stress tensor is defined as usual $\boldsymbol{\sigma} = -P\boldsymbol{I} + 2\eta \boldsymbol{e}$, and so it is the strain rate tensor $\boldsymbol{e} = \frac{1}{2}(\boldsymbol{\nabla v} + \boldsymbol{\nabla v}^T)$. The pressure field P and the variable transport coefficients λ, η and ϵ (thermal conductivity, viscosity and temperature loss coefficient, respectively) are given by

$$\begin{aligned} P &= \rho_g T f_\rho(\phi), \quad \eta = \rho_g d\sqrt{T} f_\eta(\phi), \\ \lambda &= \rho_g d\sqrt{T} f_\lambda(\phi), \quad \epsilon = (1-\varepsilon^2)\rho_g \sqrt{T} f_\epsilon(\phi)/d, \end{aligned} \tag{10}$$

where d_g is the grain diameter, ρ_g is the granular material density, ϕ is the solid volume fraction and ε the grains elastic restitution coefficient. Dimensionless functions f_ρ, f_η, f_λ and f_ϵ depend on the volume fraction and, following the work of Seguin *et al.* [20], we consider them to be approximately equal. With this assumption, transport coefficients become functions of variables P and T only,

$$\eta = \eta_0 P d/\sqrt{T}, \quad \lambda = \lambda_0 P d/\sqrt{T}, \quad \text{and } \epsilon = \epsilon_0 P/(d\sqrt{T}), \tag{11}$$

where η_0, λ_0 and ϵ_0 are dimensionless constants in the high density limit [23]. We adjusted the values of these constants to match as close as possible the experimental results.

Equations (8) and (9) are supplemented with nonslip and zero temperature gradient boundary conditions on the intruders surface, of diameter D, and a uniform flow of speed U_∞ far upstream. Seguin *et al.* [20] solved the the hydrodynamic model Eqs. (8), (9), and (11) numerically for the granular flow around a single intruder in the incompressible limit. They used finite differences for the temperature Eq. (9), and a lattice-Boltzmann model for the momentum Eq. (8). In the present work, we follow the same numerical strategy for the case of two fixed intruders immersed

in a uniform stream flow, and study their hydrodynamic interactions using a procedure for the computation of forces coming from the lattice-Boltzmann model [27].

However, it is unclear how to relate pressure on Eq. (10), with that coming from the momentum Eq. (8), since temperature is zero under uniform flow conditions and Eq. (10) will impose a corresponding zero pressure. Notice that setting a zero pressure field as an initial condition with the media at rest, may result in negative pressures during flow.

To set a base pressure level to which relate pressure with temperature through Eq. (10), we chose a characteristic base pressure from a classic solution to the Stokes flow around a cylinder [28]. The dimensionless base pressure used was $P_0 = 4/(\mathrm{Re}_i Log(7.5/\mathrm{Re}_i))$, where the initial Reynolds number is defined as $\mathrm{Re}_i = U_\infty \rho D/\eta_i < 1$, ρ is the granular media density, and η_i the initial viscosity specified below (see Section 4.10 in Ref. [29]).

To solve numerically the Eq. (9) for the temperature we scaled variables using D, U_∞ and ρ. Pressure and granular temperature are scaled with ρU_∞^2 and U_∞^2, respectively. The dimensionless equation for the granular temperature results in

$$\frac{D\theta}{Dt} = \frac{2\eta_0 d}{D}\frac{p}{\sqrt{\theta}}\boldsymbol{e} : \boldsymbol{e} + \boldsymbol{\nabla}\cdot\left(\frac{\lambda_0 d}{D}\frac{p}{\sqrt{\theta}}\boldsymbol{\nabla}\theta\right) - \frac{\epsilon_0 D}{d}p\sqrt{\theta}, \tag{12}$$

where θ and p are the dimensionless granular temperature and pressure respectively, and $\boldsymbol{e}$ is now the dimensionless strain rate tensor. Notice that the contribution from the pressure in the stress tensor term is neglected since the incompressible flow approximations is assumed, following [20], and that transport coefficients (11) in terms of the dimensionless pressure and temperature are

$$\eta = \eta_0 \rho U_\infty d\frac{p}{\sqrt{\theta}}, \quad \lambda = \lambda_0 \rho U_\infty d\frac{p}{\sqrt{\theta}}, \quad \text{and } \epsilon = \frac{\epsilon_0 \rho U_\infty}{d}\frac{p}{\sqrt{\theta}}. \tag{13}$$

Also notice that the quadratic term, the deformation contribution to the temperature increase, comes with the factor $\eta_0 p d/D\sqrt{\theta} = \eta/(\rho U D)$. This factor is the inverse of the Reynolds number Re that appears in the dimensionless momentum equation

$$\frac{D\boldsymbol{v}}{Dt} = -\boldsymbol{\nabla} p_h + \frac{1}{\mathrm{Re}}\nabla^2\boldsymbol{v}, \tag{14}$$

where the hydrodynamic pressure P computed solving the momentum equation is related to the granular model pressure by $p_h = p + p_0$ ($p_0 = P_0/\rho U_\infty^2$). Re will be considered a variable parameter, as viscosity will change in time and space with pressure and temperature.

Following Seguin *et al.* [20] we solved numerically Eq. (12) using finite differences, and Eq. (14) using a lattice Boltzmann scheme.

Numerical results and comparison with experiments

Prior to computing a solution to the coupled Eqs. (12) and (14), Eqs. (14) were first solved with a constant $\mathrm{Re} = \mathrm{Re}_i$, corresponding to a constant viscosity η_i, hence decoupled from Eq. (12). The decoupled hydrodynamic Eqs. (14) were solved until a stationary flow was obtained, to provide for an initial pressure and velocity fields to be used when coupled with the temperature Eq. (12). The computation domain is a vertical rectangle (see Fig. 6 for a close up view) with the intruders placed in the upper half. No-slip boundary conditions were imposed at the intruders surface, and a zero strain rate condition was prescribed at all but the top domain boundaries, where a uniform downward velocity of speed U_∞ was imposed. Once the initial steady flow condition was obtained, the coupled system was solved explicitly at each time step, with a zero initial temperature distribution. At the domain and intruder boundaries, zero temperature gradient conditions were used. With each time step, the pressure obtained solving Eq. (14) was applied in Eq. (12). However, each new temperature distribution will change viscosities, according to Eq. (13), and also the distribution of Re to be used in Eq. (14) for the following time step. Computations were performed until a new steady-state was obtained.

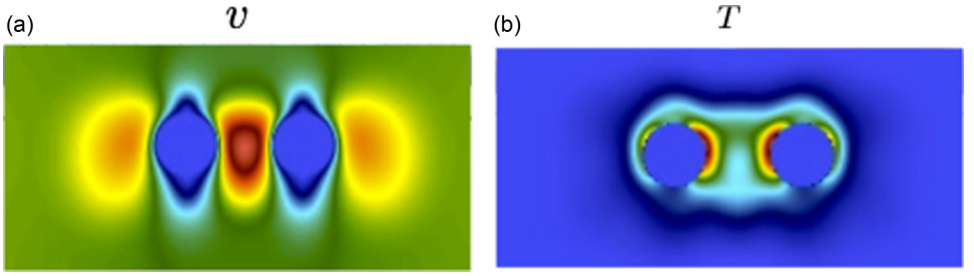

FIG. 6. Temperature and velocity fields obtained from the hydrodynamic model (LBM). Comparing these fields with the experiments [Figs. 5(a) and 5(b)] helped to find the best values of the parameters of the hydrodynamic model.

Limits were imposed over η and λ according to the numerical scheme stability conditions, especially since the temperature will remain zero in some domain regions under many circumstances. These limits override diverging coefficient values appearing in Eq. (12).

The values λ_0, ϵ_0, and η_0 for the transport coefficients Eq. (11) where chosen after exploration of different sets of values and comparison of the resulting fields and forces with the experiment. Figure 6 shows the temperature and the magnitude of the velocity computed from the model for an intruders separation of $X_{\text{sep}} = D$, $\text{Re}_i = 0.1$, $\lambda_0 = \epsilon_0 = 0.1$, and $\eta_0 = 0.005$. For comparison, Figs. 5(a) and 5(b) show experimental observations. Qualitative comparison is reasonably good, and corresponds to a regime where attraction is observed both in the experiment and in the numerical solutions.

The chosen values for λ_0, ϵ_0, and η_0 not only produce velocity and temperature fields similar to the experiments, they also reproduce reasonably well the qualitative features of attractive and repulsive interactions as a function of upstream speed and obstacles separation. Figure 7 shows the lift coefficient C_L, simply to compare with the results from the model equations for different flow velocities and obstacles separations, defined as [8]

$$C_L = \frac{\langle F_L \rangle}{\frac{1}{2}\rho_t \phi D w U_\infty^2}, \tag{15}$$

where we considered a constant packing density $\phi = 0.6$. We must stress that although the definition of the lift coefficient is the one used for high Reynolds number flows, our observations suggest a phenomena closer to a moderate Reynolds flow.

Although we are not in an inertial regime, the model equations were solved for an imposed upstream flow and no gravitational forces. The experimental data in Figs. 7(b) and 7(d) is the same data of Fig. 2 but expressed in terms of C_L to compare them to the model. In both experimental plots, we show in the main graph the data corresponding to $U_\infty \geqslant 9.4$ cm/s to better appreciate the similarity with the lift coefficient from the model. It is remarkable that not only C_L behaves as expected when separation grows, but attraction and repulsion become more intense as upstream flow diminishes, something observed in the granular system that is opposite to what happens in a Newtonian flow [3].

Quantitatively, the discrepancy between the model and the experiment on the value of the lift coefficient is large. Moreover, although the Reynolds numbers explored with the model is within the experimental range (see Fig. 7(b) of the Supplemental Material [24]), we estimate that the experimental granular Re is close to 10. This value is an order of magnitude larger than the maximum Re of the model, for which a larger Re would imply even more reduction of the intensity of attraction and repulsion.

The origin of such a sizable quantitative discrepancy is not clear for us. After exploring the space of the parameters λ_0, ϵ_0, and η_0, the chosen values are those who better reproduce the experimental

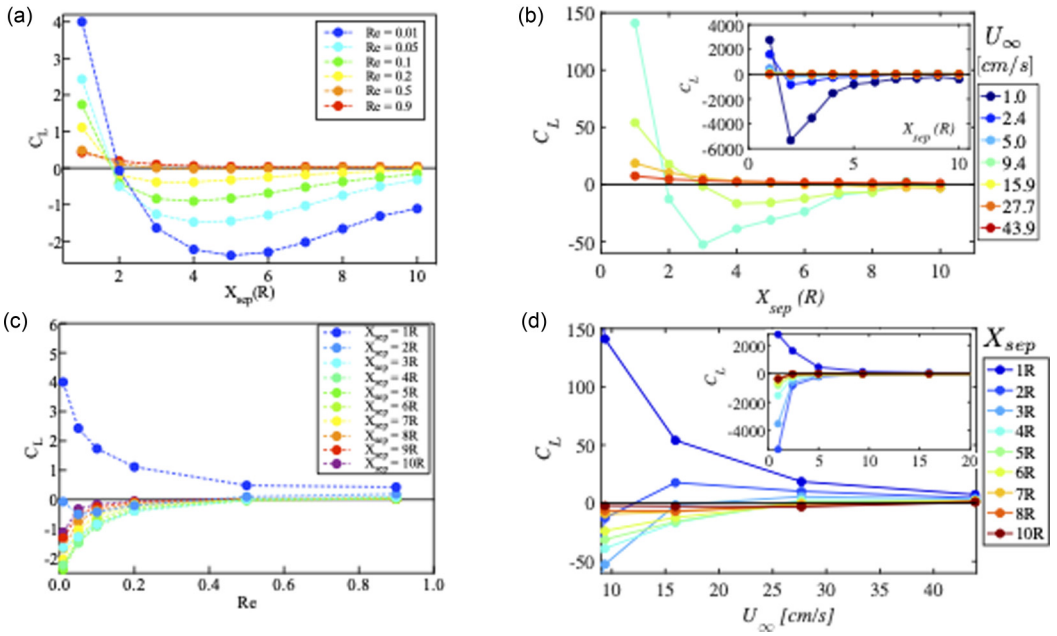

FIG. 7. Lift coefficient C_L, Eq. (15), as a function of intruders separation from (a) the LBM, and (b) experiments. In the inset in panel (b), the experimental C_L for all the flow velocities are plotted, in contrast with the main graph where only the fastest experiments are shown for clarity because the value of C_L changes dramatically with U_∞. (c) Lift coefficient from the LBM as a function of Re. (d) Experimental lift coefficient as a function of bulk velocity for $U_\infty > 9$ cm/s. Inset: lift coefficient for the whole range of U_∞.

phenomenology; we did not find a set of parameters that allowed a qualitative and quantitative match with experiments simultaneously. Noteworthy, previous works that compared experiments with this hydrodynamic model do not report a comparison of forces, they only compare velocities [20,23], most likely because in those cases the magnitude of the forces could not be adequately reproduced by the model, as happens here.

There are also some qualitative discrepancies between the model and the experiments. For example, by comparing the plots in Figs. 7(a) and 7(b) we observe that the obstacle separation at which the attraction is most substantial is smaller when flow velocity increases for the model. In contrast, for the experiment it is the other way around.

Noteworthy, if we want to give units to the velocity in the model we need to know the viscosity of the fluid equivalent to the granular material. But the viscosity depends on temperature, which behaves differently in the model and in the experiment: in the model, the temperature upstream from the intruders is zero since the the imposed upstream flow is uniform, and so the viscosity is constant, independently of the value of U_∞. In contrast, in the experiment there is a linear relation between temperature and U_∞ in the bulk far from the intruders [see Fig. 5(d)]. However, if the model were solved numerically in a three-dimensional space and the friction with the front and back walls of the container were considered, a non uniform velocity profile would be present even in the absence of intruders, and the temperature of the bulk would depend on U_∞, according to Eq. 9. Additionally, a more realistic three-dimensional model simulation will provide, through relations Eq. (10), a nonzero upstream pressure, avoiding the need of the artificial base pressure P_0 introduced with the hydrodynamic model. It would be interesting to see the behavior of the lift force and fields around the intruders in that case. Probably this would make a better quantitative match between model and experiment.

Despite these differences, it is remarkable that the model manages to capture the most important qualitative features of the phenomenology observed experimentally. This result suggests that the granular flow behaves similarly to a pair of hot obstacles immersed in a fluid with temperature-dependent viscosity, as indicated by Seguin *et al.* [20]. However, this representation has considerable limitations, and better constitutive relations are needed to describe the granular flow as a complex fluid. Understanding the reasons why the model does not manage to quantitatively describe the experimental forces can give valuable insight into the physics of dense granular rheology.

A promising set of constitutive relations to test in our system is the one recently proposed by Askari and Kamrin [30] that models the granular system as a Mohr-Coulomb material.

V. CONCLUSIONS

We report the experimental investigation of the interaction between two static objects placed side-by-side immersed in a granular flow driven by gravity. Our results confirm what we had found previously through numerical simulations in a similar geometry, namely, that attraction or repulsion exists between the intruders depending on the granular flow velocity and the distance separating the obstacles. In particular, an empirical equation obtained from the numerical simulations relating the difference in mean flow velocity at both sides of the obstacles also works well for the experimental system, even though there is a difference of two orders of magnitude in the densities of the grains used.

The experimental determination of the relation between flow velocity and granular temperature allowed us to make a gross estimate of the possible value of the granular Reynolds number for our system, although the resulting range of possible values is too large (four orders of magnitude) to be useful. A refinement of this estimation is needed to make relevant comparisons with hydrodynamic models.

We successfully adapted to our system the Lattice-Boltzmann scheme to solve a hydrodynamic model, and we found a remarkable sound qualitative reproduction of the experimental velocities, temperatures, and forces. The quantitative discrepancies suggest that the constitutive relations of the model are not entirely correct and that better relationships must be found.

Systematic variations of quantities like the dimensions of the system and the size of grains and obstacles will help to unravel the origin of long-range interactions within a granular flow. It also rests as an open question the understanding of the empirical Eq. (5) and a study of the role of velocity fluctuations on attraction and repulsion.

Finally, the ranges of Froude and Inertia numbers show that the granular flow in our experiments is in a quasistatic regime for low velocities and transits to an intermediate regime at larger flow velocities. This, together with the fact that the attraction between obstacles is maximized at low velocities suggest that energy dissipation governs the forces in this system and not only inertia, and, consequently the attractive lift cannot be a Bernoulli-like force. The observed qualitative agreement of the hydrodynamic model is encouraging and supports the search of models that include both viscous and inertial effects.

ACKNOWLEDGMENTS

This work has been supported by Conacyt, Mexico, under Grant Ciencia Básica 180873. M.F.A.-E. thanks Conacyt, Mexico, for postdoctoral financial support. We gratefully acknowledge the support of NVIDIA Academic Hardware Grant Program for the donation of the Titan V GPU used for this research.

[1] L. V. Wijngaarden and D. J. Jeffrey, Hydrodynamic interaction between gas bubbles in liquid, J. Fluid Mech. **77**, 27 (1976).

[2] R. A. L. de la Cruz and G. A. Caballero-Robledo, Lift on side-by-side intruders within a granular flow, J. Fluid Mech. **800**, 248 (2016).
[3] I. Kim, S. Elghobashi, and W. A. Sirignano, Three-dimensional flow over two spheres placed side by side, J. Fluid Mech. **246**, 465 (1993).
[4] D. Legendre, J. Magnaudet, and G. Mougin, Hydrodynamic interactions between two spherical bubbles rising side by side in a viscous liquid, J. Fluid Mech. **497**, 133 (2003).
[5] V. Buchholtz and T. Pöschel, Interaction of a granular stream with an obstacle, Granular Matter **1**, 33 (1998).
[6] C. R. Wassgren, J. A. Cordova, R. Zenit, and A. Karion, Dilute granular flow around an immersed cylinder, Phys. Fluids **15**, 3318 (2003).
[7] J. E. Hilton and A. Tordesillas, Drag force on a spherical intruder in a granular bed at low Froude number, Phys. Rev. E **88**, 062203 (2013).
[8] T. Faug, Macroscopic force experienced by extended objects in granular flows over a very broad Froude-number range, Eur. Phys. J. E **38**, 34 (2015).
[9] F. Moro, T. Faug, H. Bellot, and F. Ousset, Large mobility of dry snow avalanches: Insights from small-scale laboratory tests on granular avalanches of bidisperse materials, Cold Reg. Sci. Technol. **62**, 55 (2010).
[10] M. R. Shaebani, J. Sarabadani, and D. E. Wolf, Nonadditivity of Fluctuation-Induced Forces in Fluidized Granular Media, Phys. Rev. Lett. **108**, 198001 (2012).
[11] J. M. Ottino and D. V. Khakhar, Mixing and segregation of granular materials, Annu. Rev. Fluid Mech. **32**, 55 (2000).
[12] C. Cattuto, R. Brito, U. M. B. Marconi, F. Nori, and R. Soto, Fluctuation-Induced Casimir Forces in Granular Fluids, Phys. Rev. Lett. **96**, 178001 (2006).
[13] D. A. Sanders, M. R. Swift, R. M. Bowley, and P. J. King, Are Brazil Nuts Attractive? Phys. Rev. Lett. **93**, 208002 (2004).
[14] I. Zuriguel, J. F. Boudet, Y. Amarouchene, and H. Kellay, Role of Fluctuation-Induced Interactions in the Axial Segregation of Granular Materials, Phys. Rev. Lett. **95**, 258002 (2005).
[15] S. Aumaître, C. A. Kruelle, and I. Rehberg, Segregation in granular matter under horizontal swirling excitation, Phys. Rev. E **64**, 041305 (2001).
[16] F. Pacheco-Vazquez and J. C. Ruiz-Suarez, Cooperative dynamics in the penetration of a group of intruders in a granular medium, Nat. Commun. **1**, 123 (2010).
[17] M. Dhiman, S. Kumar, K. A. Reddy, and R. Gupta, Origin of the long-ranged attraction or repulsion between intruders in a confined granular medium, J. Fluid Mech. **886**, A23 (2020).
[18] J. M. Solano-Altamirano, G. A. Caballero-Robledo, F. Pacheco-Vázquez, V. Kamphorst, and J. C. Ruiz-Suárez, Flow-mediated coupling on projectiles falling within a superlight granular medium, Phys. Rev. E **88**, 032206 (2013).
[19] D. Yang, N. Gravish, and D. I. Goldman, Drag Induced Lift in Granular Media, Phys. Rev. Lett. **106**, 028001 (2011).
[20] A. Seguin, Y. Bertho, P. Gondret, and J. Crassous, Dense Granular Flow Around a Penetrating Object: Experiment and Hydrodynamic Model, Phys. Rev. Lett. **107**, 048001 (2011).
[21] B. Andreotti, Y. Forterre, and O. Pouliquen, *Granular Media: Between Fluid and Solid* (Cambridge University Press, Cambridge, UK, 2013).
[22] J. T. Jenkins and S. B. Savage, A theory for the rapid flow of identical, smooth, nearly elastic spherical particles, J. Fluid Mech. **130**, 187 (1983).
[23] L. Bocquet, W. Losert, D. Schalk, T. C. Lubensky, and J. P. Gollub, Granular shear flow dynamics and forces: Experiment and continuum theory, Phys. Rev. E **65**, 011307 (2001).
[24] See Supplemental Material at http://link.aps.org/supplemental/10.1103/PhysRevFluids.6.084303 for more details of the experimental setup; drag force measurements; comparison of lift force on the left and right intruders; details on fields measurements; Froude, Inertia, and Reynolds numbers estimation [31–34]; the hydrodynamic model [27,35–38]; snapshots of velocity and temperature fields for different velocities and separations; and movies of the flow at different velocities and separations.

[25] M. F. Acevedo-Escalante and G. A. Caballero-Robledo, Lift on side by side intruders of various geometries within a granular flow, EPJ Web Conf. **140**, 03048 (2017).
[26] The threshold in the value of the number I that is usually considered for the quasistatic regime is $I \lesssim 10^{-3}$, although this value depends strongly on the geometry of the system [39], and some authors report the quasistatic regime for $I \leqslant 10^{-2}$ and the collisional regime for $I \geqslant 0.2$ [40].
[27] R. Mei, D. Yu, W. Shyy, and L. Luo, Force evaluation in the lattice Boltzmann method involving curved geometry, Phys. Rev. E **65**, 041203 (2002).
[28] H. Lamb, On the uniform motion of a sphere through a viscous fluid, Phil. Mag. **21**, 112 (1911).
[29] G. K. Batchelor, *Introduction to Fluid Dynamics* (Cambridge University Press, Cambridge, UK, 1967).
[30] H. Askari and K. Kamrin, Intrusion rheology in grains and other flowable materials, Nat. Mater. **15**, 1274 (2016).
[31] G. D. Scott and D. M. Kilgour, The density of random close packing of spheres, J. Phys. D **2**, 863 (1969).
[32] P. See-Eng, W. B. Russel, J. Zhu, and P. M. Chaikin, Effects of polydispersity on hard sphere crystals, J. Chem. Phys. **108**, 9789 (1998).
[33] F. R. S. and G. R. D., Close packing density of polydisperse hard spheres, J. Chem. Phys. **131**, 244104 (2009).
[34] B. Vasili and T. Ulrich, Random-close packing limits for monodisperse and polydisperse hard spheres, Soft Matter **10**, 3826 (2014).
[35] H. Xiaoyi and L. Li-Shi, Lattice Boltzmann Model for the Incompressible Navier-Stokes Equation, J. Stat. Phys. **88**, 927 (1997).
[36] F. Mandujano and R. Rechtman, Thermal levitation, J. Fluid Mech. **606**, 105 (2008).
[37] Z. Guo, C. Zheng, and S. B, An extrapolation method for the boundary conditions in the lattice Boltzmann method, Phys. Fluids **14**, 2007 (2002).
[38] F. Mandujano and C. Málaga, On the forced flow around a rigid flapping foil, Phys. Fluids **30**, 061901 (2018).
[39] A. L. Thomas, Z. Tang, K. E. Daniels, and N. M. Vriend, Force fluctuations at the transition from quasistatic to inertial granular flow, Soft Matter **15**, 8532 (2019).
[40] F. da Cruz, S. Emam, M. Prochnow, J.-N. Roux, and F. Chevoir, Rheophysics of dense granular materials: Discrete simulation of plane shear flows, Phys. Rev. E **72**, 021309 (2005).